Environmental Earth Sciences (2024) 83:219
https://doi.org/10.1007/s12665-024-11479-4

ORIGINAL ARTICLE

The study of mineral distribution using hyperspectral Hyperion data along the shores of Lake Salda/Türkiye

Mehmet Ali Akgül[1,2] · **Suphi Ural**[3]

Received: 4 August 2023 / Accepted: 3 February 2024
© The Author(s) 2024

Abstract

Lake Salda is considered the most similar region on Earth to search for evidence of life on Mars, and its shoreline is home to microbialites containing some of the oldest known fossilized records of life on our planet. Understanding the historical process of Mars is also crucial for predicting the future of our planet, given its transition from a watery world to an arid one. In mineralogical studies to be carried out in sensitive areas such as private protected areas, it is a priority not to damage the area, and mineralogical research using remote sensing methods is frequently used in such studies. In this study, the mineralogical characteristics of the geological formations in and around Kocaadalar Burnu peninsula, located in the southwest of Lake Salda, were examined using remote sensing techniques. Mineral studies of Lake Salda were conducted using data from the Hyperion data of the Earth Observation-1 (EO-1) satellite, which can detect in 220 bands between 357 and 2576 nm wavelengths which is capable of hyperspectral sensing. The EO-1 satellite, the first spacecraft of NASA's New Millennium Programme, which operated successfully from its launch in 2000 until the end of its mission in 2017, carried the multispectral Advanced Land Imager and LEISA Atmospheric Corrector sensors, in addition to the Hyperion hyperspectral sensor. The Hyperspectral Material Identification tool in the Tactical Hyperspectral Operations Resource module of the ENVI software, the United States Geological Survey spectral library, and the Adaptive Coherence Estimator algorithm were used in the study. According to the results of this study conducted on the shores of Lake Salda, in addition to the hydromagnesite mineral, the existence of which was previously detected by various researchers, trona, vermiculite, rivadavite and borate minerals such as ulexite, tincalconite and colemanite were also detected. The results of this study have shown that remote sensing methods can make significant contributions to research in special protected areas such as Lake Salda. It is thought that the presence of trona and boron minerals in the region will contribute positively to the understanding of the historical process of Salda Lake.

Keywords Hyperspectral remote sensing · Mineralogy · Lake Salda · Trona · Borates

Introduction

Remote sensing methods are utilized in numerous industries, including agriculture, environment, urban planning, meteorology, and disaster management. Additionally, these methods are commonly implemented within the realm of earth sciences such as mining, geology, and mineralogy. For conducting mineralogical studies in environmentally sensitive areas, including special conservation areas, protection of the area is crucial. Remote sensing techniques are commonly utilized in such studies to avoid the possibility of any damage to the area.

Lake Salda, a medium-sized crater lake in southwestern Türkiye, which came to prominence with the Jezero Crater on Mars, was considered the most similar region on Earth

✉ Mehmet Ali Akgül
mali.akgul@dsi.gov.tr

Suphi Ural
suralp@cu.edu.tr

[1] Geographic Information Systems Section, Department of Information Technologies, General Directorate of State Hydraulic Works, 6Th Regional Directorate, Adana, Türkiye

[2] Department of Remote Sensing and Geographic Information Systems, Institute of Natural and Applied Sciences, Çukurova University, Adana, Türkiye

[3] Department of Mining Engineering, Çukurova University, Adana, Türkiye

Published online: 30 March 2024

to look for evidence of life on Mars (Horgan et al. 2020). The first goal of the Perseverance rover, which explores Jezero Crater, is to identify past environments that can support microbial life and to look for signs of possible past microbial life. In this regard, Lake Salda, whose shoreline is formed by microbialites, has been the focus of research (Garczynski et al. 2019).

Russell et al. (1999) report that hydromagnesite stromatolites are formed in and around Kocaadalar Burnu peninsula, Salda Lake provide excellent opportunities for study of carbonate morphologies in preparation for an exobiological exploration of Mars. Kazancı et al. (2004) examined the limnological characteristics of Lake Salda, which is a deep, soda and highly alkaline lake.

Wang and Zheng (2010) used the Support Vector Machine (SVM) classification method in their study using EO-1 Hyperion hyperspectral data from BeiYa region in northwestern YunNan Province, China. Because of their study, they found that alteration zones can be identified very effectively with Hyperion data and that the mineralogical and lithological information generated from these data is largely consistent with the geological map and previous research results.

Salaj et al. (2012) used Hyperion data to map mineral abundance in Udaipur region of Rajasthan, India. They used Blend Adjustment Matched Filtering and Spectral Angle Mapper (SAM) methods in their study, using FLAASH software and the United States Geological Survey (USGS) mineral library. They concluded that although the spatial distribution of minerals is influenced by topographic effects and vegetation cover, Hyperion data are useful for determining mineral abundance and mapping geologic features.

Pour and Hashim (2014) used Landsat ETM+ and Hyperion satellite data to perform mineral mapping in the study area and surrounding terrain in the Bau gold mining area in the state of Sarawak, East Malaysia, Borneo Island. Because of the study, they have demonstrated the importance and advantages of using ETM+ and Hyperion remote sensing data together to identify potential areas in tropical/subtropical regions. They also demonstrated that indicators of structurally controlled gold mineralization, including iron oxides, clay minerals, faults, and fractures in the Bau gold mining area, can be detected using satellite remote sensing data.

Ducart et al. (2016) conducted a study using remote sensing methods in Serra Norte iron deposits in Caracas, Brazil. They used the EO-1/Hyperion satellite data as satellite images, and used the Spectral Angle Mapper (SAM) classification method. As a result of the study, they obtained good results in mapping high-grade iron ore, hematite–goethite, and clay minerals of regolith origin, and stated that EO-1/Hyperion imagery is an excellent tool for rapid mineral mapping in open pit areas, as well as for mapping waste and waste disposal facilities.

Oskouei and Babakan (2016) used Hyperion satellite data and a standardized hyperspectral processing method developed by Analytical Imaging and Geophysics (AIG) to map the mineral distribution in the study area in the Lahroud region of Ardabil province, northwestern Iran. As a result of the study, they found that the mineral distribution maps they produced were in high agreement with the geological map of the region. They also stated that it can be successfully used to reveal the mineralization trend in the region.

Balcı et al. (2018) investigated the geomicrobiology of Lake Salda and stated that stromatolites forms under a complex biological, chemical and physical biogeochemical processes and also indicate that bacteria serve as a nucleation site and control kinetic factors such as precipitation rate by lowering activation energy rather than thermodynamic factors (e.g. alkalinity, pH). Garczynski et al. (2019) reported that Lake Salda is good compositional analogs for a Jezero paleolake.

Kah et al. (2020) investigated the mineralogy of authigenic and detrital sediments of Salda Lake to understand the nature of carbonate accumulation in the Jezero crater. As a result of this study, it is reported that hydromagnesite is rare in deltas and is associated with paleo-shorelines, and the formation of darker-toned Fe/Mg-smectite muds in Salda Lake may be due to groundwater or stream input, but further studies are needed to confirm the formation mechanisms.

Varol et al. (2020) investigated the geological, hydrological, hydrogeological and hydrochemical characteristics of water resources in the south of the Salda Lake basin. The results of this investigation showed that groundwater and surface waters are in the Mg-Ca-HCO_3 and Ca-Mg-HCO_3 facies.

Bouzidi et al. (2022) conducted a study at the Tamera open pit mine in the Nefza mining district of northwestern Tunisia, which shows strong potential for heavy iron mineralization. They examined iron oxide mineralization using EO-1 Hyperion hyperspectral data and compared laboratory analyzes of 56 samples with satellite data. As a result of their study, they demonstrated the presence of a mineralogical composition consisting primarily of iron oxide minerals (hematite and goethite) and minerals such as clays (kaolinite) in all samples.

Kaya et al. (2023) investigated trace and Rare Earth Element, geochemistry of recently formed stromatolites at Lake Salda. One of the results of this study indicated that hydromagnesite composition of the Salda Lake stromatolites were precipitated from the waters influenced by Mg-rich meteoric waters fed from the serpentinite rocks around the Lake.

In this study, the mineral distribution in Lake Salda was studied using the Hyperion sensor data on the EO-1 satellite capable of hyperspectral sensing, the HMI tool in the THOR module within the ENVI software, the USGS spectral library, and the ACE algorithm.

Materials and methods

Study area

Lake Salda is a somewhat salty karst lake in the Yeşilova district of Burdur, Türkiye, 4 km from the district seat. It is flanked by forest-covered hills, stony terrain, and tiny alluvial plains. The Lake Salda basin is located between 37° 30′ 33″ and 37°35′10″ northern latitudes and 29° 38′ 28″ and 29° 43′ 34″ east longitudes in the geographical coordinate system. In the Lakes Region, it has a closed basin structure with no outflow. It is Türkiye's third deepest lake, with a surface size of around 44 km^2 and a depth of up to 184 m. In this study, an area of approximately 57 hectares in size in and around the peninsula of Kocaadalar Burnu, located on the southwest shore of Lake Salda, was examined. The altitude of the study area is 1145 m above sea level, it has a flat topography and no vegetation. (Fig. 1).

Lake Salda was designated and declared a Special Environmental Protection Area by the President's Decision dated 14.03.2019 and numbered 824, which was published in the Official Gazette on 15.03.2019 and numbered 30,715.

Lake Salda is a tectonically-formed lake that began to form at the end of the Neogene period and took on its present shape as a result of subsequent tectonic movements (Akkuş 1987). The accumulation of surrounding waters in an anticline area and a segment where the fold axes decline led to the initial formation of the lake (Altınlı 1955). The structure is situated in the "Taurus Tectonic Union" of Anatolia's tectonic units. It was formed during the Alpine Orogenesis and is occasionally found among serpentinised ophiolites. Limestones are exclusively present on the Kale hill north of Kaledibi village, southeast of the lake. The lake's surrounding is made up of Peridotides, which at times are found alongside limestones from the Mesozoic era (Erentöz 1974). The geological map of the study area made by the Institute of Mineral Research and Exploration (MTA) is given in Fig. 2.

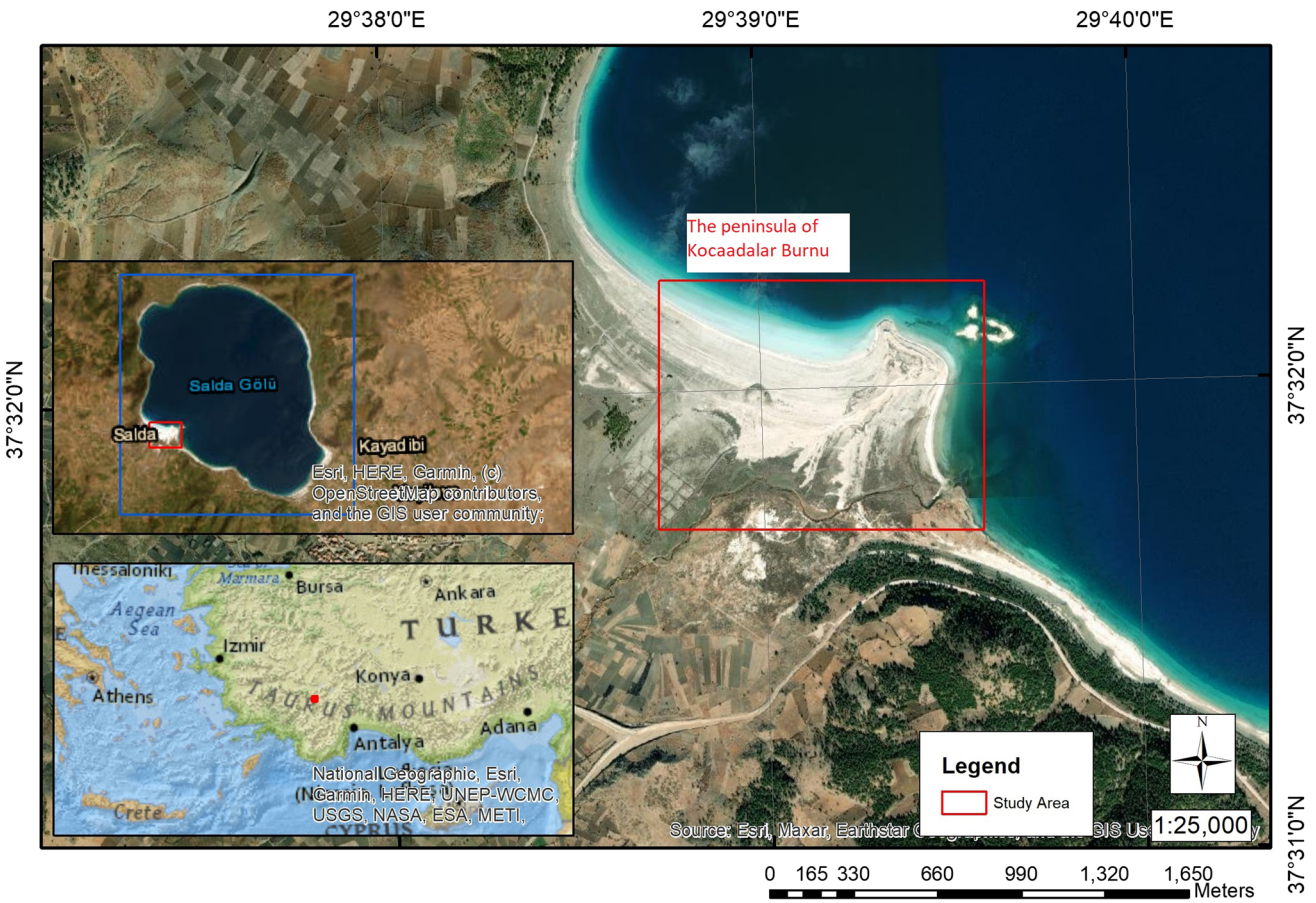

Fig. 1 Study area

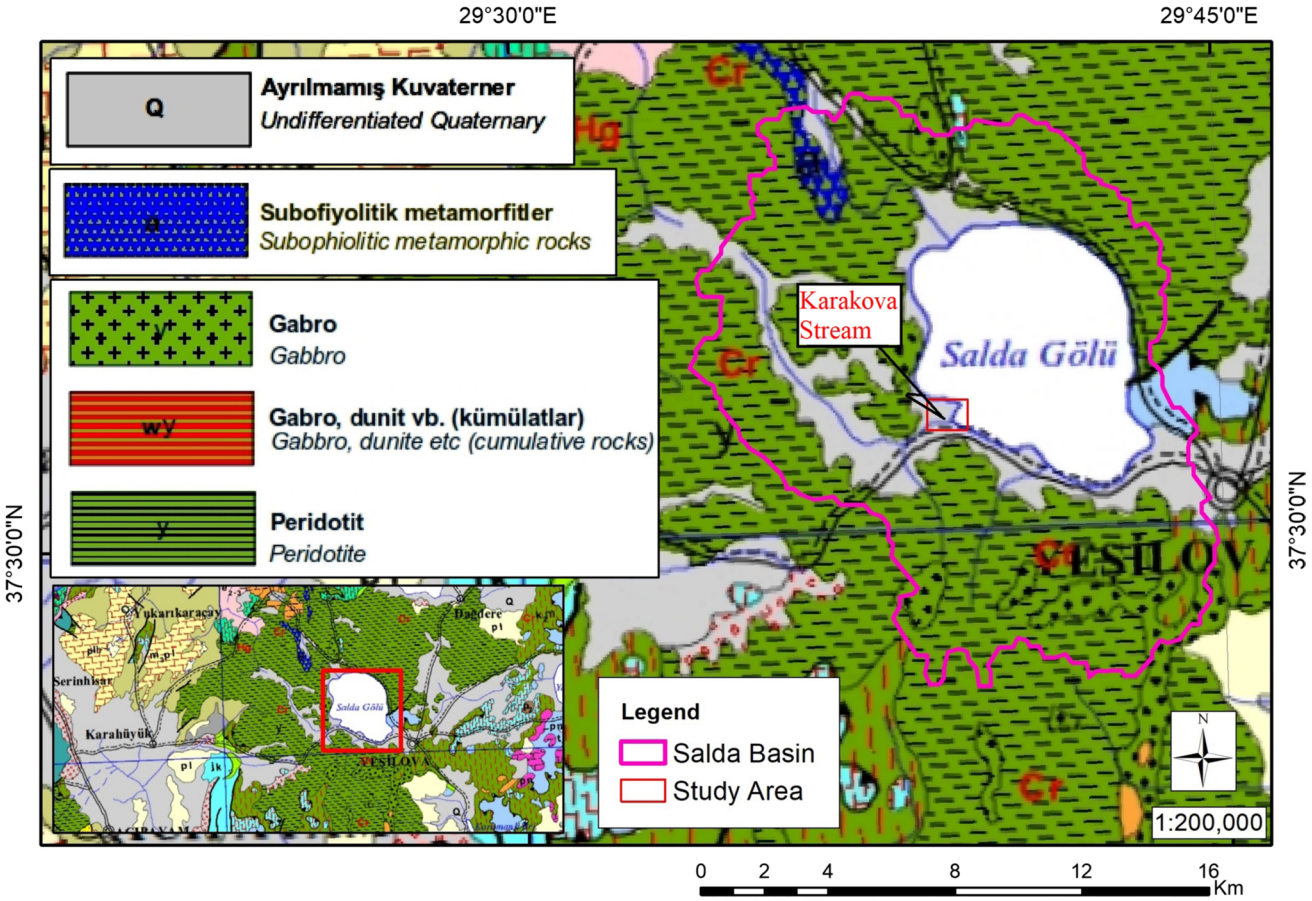

Fig. 2 Study area geological map (MTA 2023)

Materials

The Earth Observing Mission-1 (EO-1) satellite, launched by the United States on a Delta II rocket from Vandenberg Air Force Base on November 21, 2000, was the first spacecraft of the American New Millennium Program (NMP) (NASA 2023). The EO-1 satellite has three instruments: the hyperspectral Hyperion instrument, which we used in this study, the multispectral Advanced Land Imager (ALI) instrument, and the LEISA Atmospheric Corrector (LAC) instrument. The Hyperion instrument has a spatial resolution of 30 m and can detect in 220 spectral bands from 0.4 to 2.5 µm. The ALI instrument was a multispectral sensor with the same spatial resolution as Hyperion and can detect in 10 spectral bands from 0.4 to 2.4 µm. The LAC instrument covers the 0.89–1.6 µm wavelength IR band using a wedged etalon filter and three arrays of In-Ga detectors, each array providing 250 m spatial resolution (Barry 2001).

There are 220 unique spectral channels captured with a total spectral range of 357–2576 nm. The Level 1 radiometric product has a total of 242 bands, but only 198 are calibrated. There are only 196 unique channels due to overlap between the VNIR and SWIR focal planes. Calibrated channels are 8–57 for VNIR and 77–224 for the SWIR. The lack of calibration of all 242 channels was mostly due to the low sensitivity of the detectors. In some channels, the uncalibrated bands are set to zero (Beck 2003). The characteristics of the Hyperion data used in the study are shown in Table 1, and the footprint of the satellite is shown in Fig. 3.

Hyperion data are processed on three different levels: L1R, L1Gst and L1T. At the L1R level, radiometric corrections were applied to the images, while at the L1Gst level, in addition to the L1R level, a 90-m digital elevation model (DEM) was used for topographic accuracy and systematic geometric corrections were applied from spacecraft ephemeris data. At the L1T level, radiometric and systematic geometric corrections including ground control points were applied in addition to the L1Gst level for geodetic accuracy (Simon and Beckman 2006; USGS 2021). Since only the L1R and L1Gst levels of the study area are available in this study, the L1Gst data, which have increased topographic accuracy through the use of DEM data, were used in addition to the L1R level data. Hyperion data were acquired from EarthExplorer, an online platform

Table 1 Hyperion instrument specifications (Beck 2003)

Instrument	Specifications	Instrument	The number of bands
Spectral range	0.4–2.5 µm	Visible bands	35
Spatial resolution	30 m	Near infrared bands	35
Swath width	7.5 km	Short wave infrared	172
Spectral coverage	Continuous	Panchromatic bands	0
Pan band resolution	N/A	Middle infrared bands	0
Stereo	No	Thermal band	0
The number of spacecraft	1	Total bands	220
Temporal resolution	200 days		

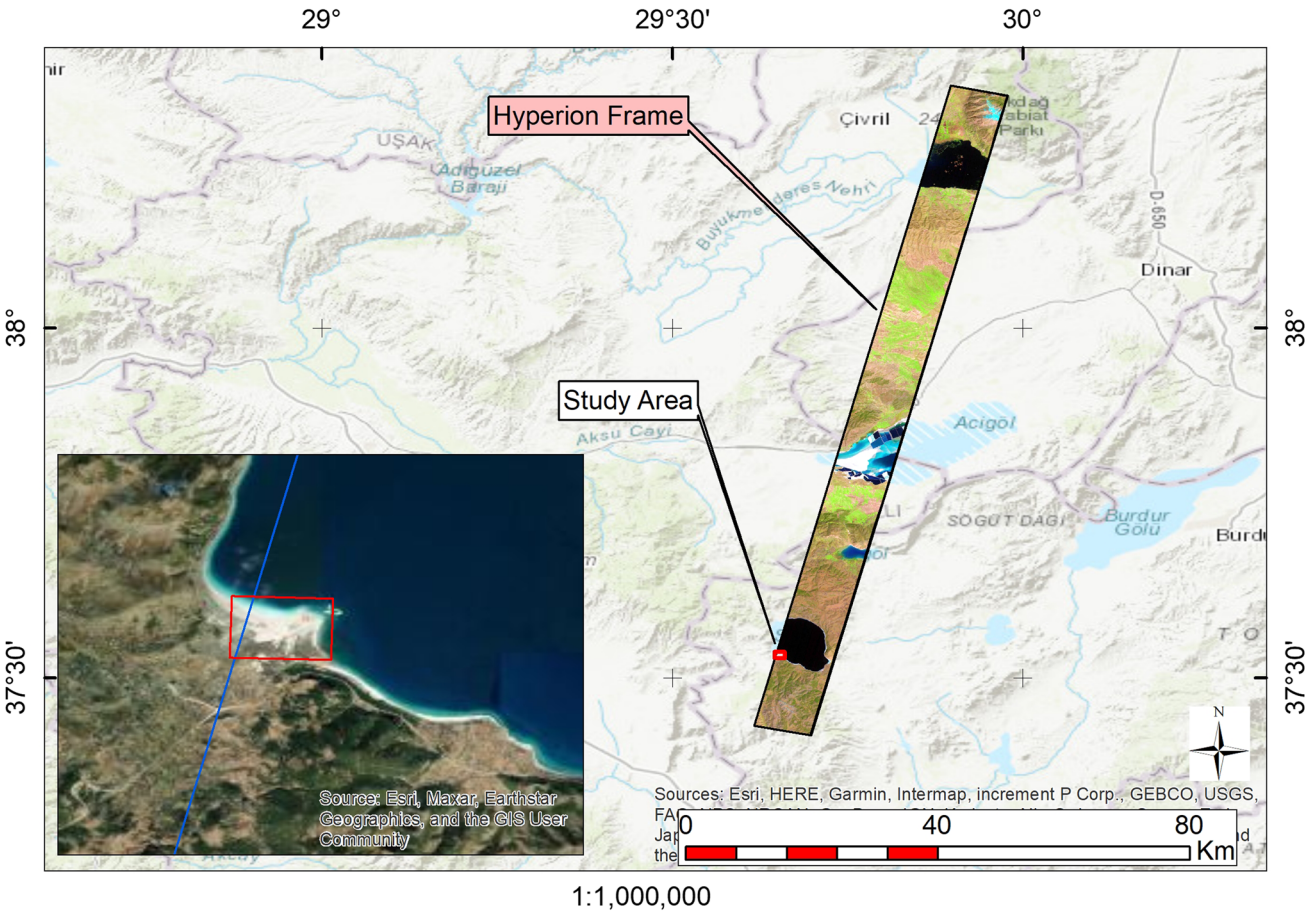

Fig. 3 Hyperion image footprint

Table 2 The name of the Hyperion image and date, used in the study

Image name	Date
EO1H1790342010095110PV_SGS_01	05/04/2010

that facilitates online search, browsing, metadata exportation, and data downloading for earth science data archived by the USGS. As a result of the archive search, it was determined that there was only one image in the study area. The name and date of this image are listed in Table 2 (USGS 2023).

Methods

The Environment for Visualizing Images (ENVI) software was used to perform radiometric and atmospheric corrections on the Hyperion data, which can detect at 357 and 2576 nm wavelengths and 30 m resolution in 220 bands used in the study. ENVI is a software with advanced image processing capabilities that allows meaningful information to be extracted from a wide range of data. In hyperspectral satellites, some bands can cause significant interference, particularly at wavelengths associated with atmospheric absorption and water vapor. These bands must be removed before analysis. In EO-1 Hyperion data, bands 1–7, 58–76, and 221–242 are automatically set to 0 by the data provider (Barry 2001). Also, as noted by Datt et al. (2003), bands 121–126 and 167–180 were removed in the preprocessing step due to the strong noise generation corresponding to strong water vapor absorption.

After removing the bad bands, the radiometric corrections necessary to use the image were calculated using the ENVI software, and the Quick Atmospheric Correction (QUAC) module of the same software was used for the atmospheric corrections calculated according to Canty (2014). QUAC is a scene-based empirical method that converts radiance values to apparent surface reflectance. Scene-based means that the atmospheric correction parameters are derived strictly from the pixel spectra within the scene and not from ancillary data (Bernstein et al. 2005, 2012). Mineral analysis of radiometrically and atmospherically corrected images was performed using the Hyperspectral Material Identification (HMI) tool in the Tactical Hyperspectral Operations Resource (THOR) module of the ENVI software.

In the THOR HMI analysis, the United States Geological Survey (USGS) spectral library was used and the best matching minerals were determined using the Adaptive Coherence Estimator (ACE) algorithm. Hyperspectral Material Identification (HMI) tool in the Tactical Hyperspectral Operations Resource (THOR) module of the ENVI software generally focuses on qualitative mineral identification. It helps identify and classify materials based on their spectral signatures.

The USGS spectral library contains a collection of spectra collected with laboratory, field, and airborne spectrometers (Clark et al. 2007). The wavelengths covered by the instruments range from ultraviolet to far infrared (0.2–200.0 µm) (Kokaly et al. 2017). The spectra in the library were measured using four different types of spectrometers, and data from the Beckman^{TM} 5270 spectrometer in the 0.2–3.0 m spectral range were used in this study.

The ACE technique identifies whether a pixel spectrum could contain a known target signature. This is particularly useful when the conditions of the background are uncertain and varied. It is not affected by the scaling of input spectra, and all the end members in the scene do not need to be known (Manolakis et al. 2003; Kraut et al. 2005). Its performance is reliable in the detection of sub-pixel targets (Wolfe and Black 2018). The ACE algorithm is used for the mineral that is dense in the pixel. ACE values range from − 1 to 1, with values close to 1 indicating the best match (Nv5 2023). This study was conducted according to the flow chart shown in Fig. 4.

The examined points were created using the ArcMap program (ESRI 2011). For analysis, 634 points were constructed based on the midpoint of each pixel of Hyperion data with a spatial resolution of 30 m (Fig. 5).

Results and discussion

ACE values for each pixel were calculated separately for all 428 minerals in the "Minerals" category of the USGS spectral library. In addition, hydromagnesite, which is not in the "Minerals" category of the USGS spectral library, but in the "Soils and Mixtures" category, was also analyzed. Hydromagnesite has been reported to occur frequently in this region, which is the reason for this analysis.

ACE levels between 0.9 and 1.0 are very acceptable, good between 0.75 and 0.9, poor-appropriate between 0.5 and 0.75, and inappropriate for values less than 0.5 (Nv5 2023). Minerals with ACE values greater than 0.75 are given in Table 3. There were 23 minerals with ACE values greater than 0.75, 202 minerals with values between 0.5 and 0.75, and 203 minerals with values less than 0.5.

Figure 6 shows the wavelength plot in the USGS spectral library of six minerals that have a distribution greater than 5% in the study area, as well as the wavelength plot of the Hyperion pixel that has the largest distribution in the ACE analysis. Since the hydromagnesite ($Mg_5(CO_3)_4(OH)_2{\cdot}4H_2O$) was detected in all pixels, it is not included here.

Trona mineral with the chemical formula $Na_3H(CO_3)_2$ $2H_2O$ (Chukanov 2014) is shown in Fig. 6a, ulexite mineral with the chemical formula $NaCaB_5O_9$ $8H_2O$ (Korbel and Novák 2001) is shown in Fig. 6b, tincalconite mineral with the chemical formula $Na_2(B_4O_7)$ $5H_2O$ (Kokaly et al. 2017) is shown in Fig. 6c, vermiculite mineral with the chemical formula $(Mg,^{Fe+2},Al)_3((Al,Si)_4O_{10})(OH)_2$ $4H_2O$ (Kokaly et al. 2017) is shown in Fig. 6d, colemanite mineral with the chemical formula $Ca_2B_6O_{11}$ $5H_2O$ (Kokaly et al. 2017) is shown in Fig. 6e, rivadavite mineral with the chemical Formula $Na_6MgB_{24}O_{40}$ $22H_2O$ (Kokaly et al. 2017) is shown in Fig. 6f.

The band depths of the minerals detected as a result of ACE analysis and whose wavelength graphs are given in Fig. 6 were also analyzed to determine at which wavelengths they were absorbed. Band depth (absorption) is one of the most widely used methods in the parameterisation of spectral data (Clark and Roush 1984). For this purpose, the

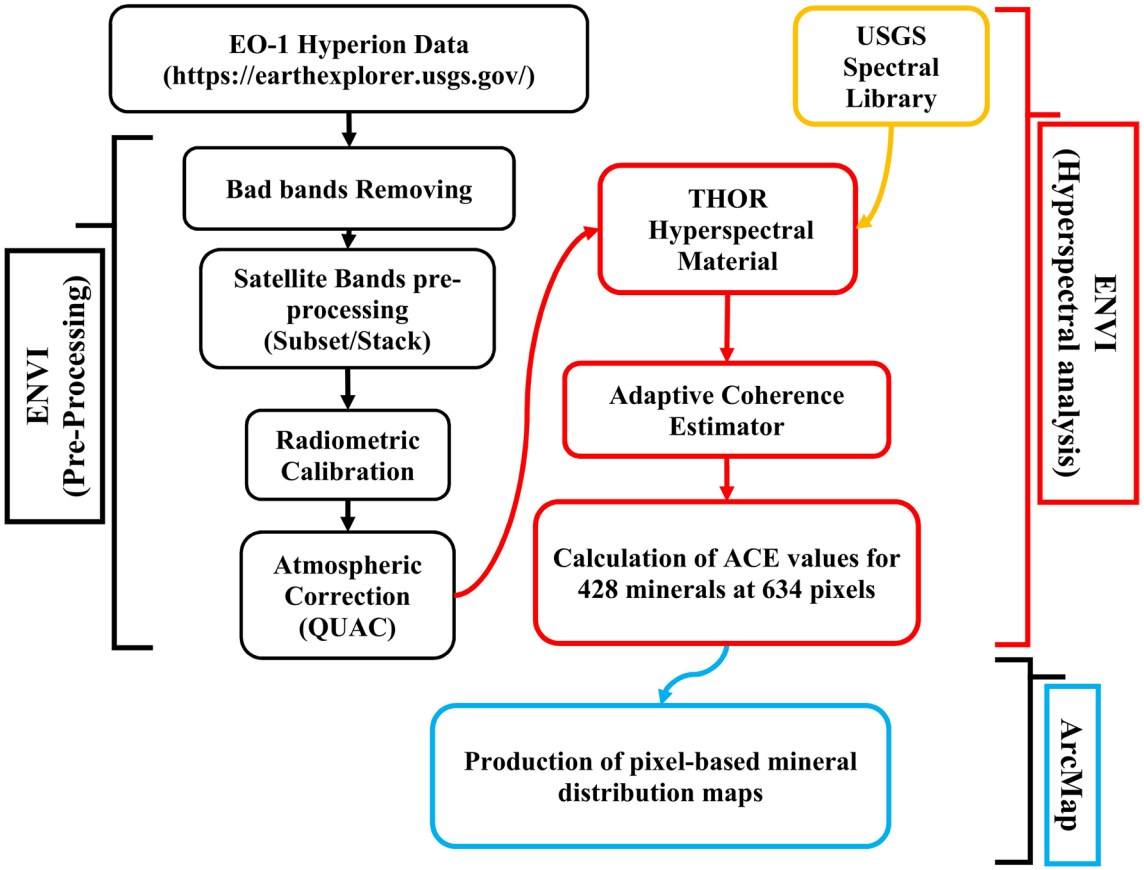

Fig. 4 Flowchart of the study

wavelength of the pixel where the minerals are most intense was removed and shown as "Continuum Removed" (Fig. 7). The Continuum Removed method normalises the wavelength by comparing it to a continuum curve, thus defining a common baseline for measuring absorption feature depth and position. A continuum curve is a mathematical function created by fitting a convex hull to the spectrum. The resulting reflection curve gives a better picture of band centres and depths (Wolfe and Black 2018). As a result of the analyses, the wavelengths at which the minerals are absorbed in the most intense pixel and the graph showing the wavelengths absorbed by the minerals taken from the USGS spectral library are shown in Fig. 7.

Analysis reveals that the examined area consists of hydromagnesite along with trona and borates such as ulexite, tincalconite and colemanite. Hydromagnesite mineral ($Mg_5(CO_3)_4(OH)_2{\bullet}4H_2O$) is detected in all of the study area as a result of ACE analysis. Trona ($Na_3H(CO_3)_2\ 2H_2O$) detected in 35% of the study area as a result of ACE analysis. The mineral was detected with higher values in the northern part of the study area, starting at a distance of approximately 100 m from the shore of Lake Salda and inland. In the eastern part of the study area, it was detected inland at a distance of approximately 250 m from the shore (Fig. 8a). Trona deposits, which have a limited distribution in the Earth's crust, can be found in unusual concentrations in some places, usually together with borate and other salt deposits. Their origin is related to alkaline volcanism, hot spring activity, closed basins, and arid climate, and Quaternary sodium carbonate minerals (trona minerals) are found in salars, playa lakes such as Lake Van, and salt lakes (Helvacı 2019a).

According to ACE analysis, ulexite ($NaCaB_5O_9\ 8H_2O$) mineral is found in 26.2% of the study area, 50 m away from the beach and in the central parts of the study area. (Fig. 8b). Ulexite, an evaporite mineral commonly found with colemanite in sedimentary rocks in areas where borax deposits occur (Korbel and Novák 2001). Balcı et al. (2018) reported that Na_2O and Boron (B) was detected in 10 different samples taken from the Salda Lake sediments, hydromagnesite terrace and Kocaadalar Burnu peninsula. Typically, in playa and salt marsh deposits in arid regions, and in bedded sedimentary deposits formed from them, boron is supplied by surrounding hot springs (Anthony et al. 2003). Although many minerals contain boric oxide, the three most commercially important minerals in the world are borax, ulexite, and colemanite, which

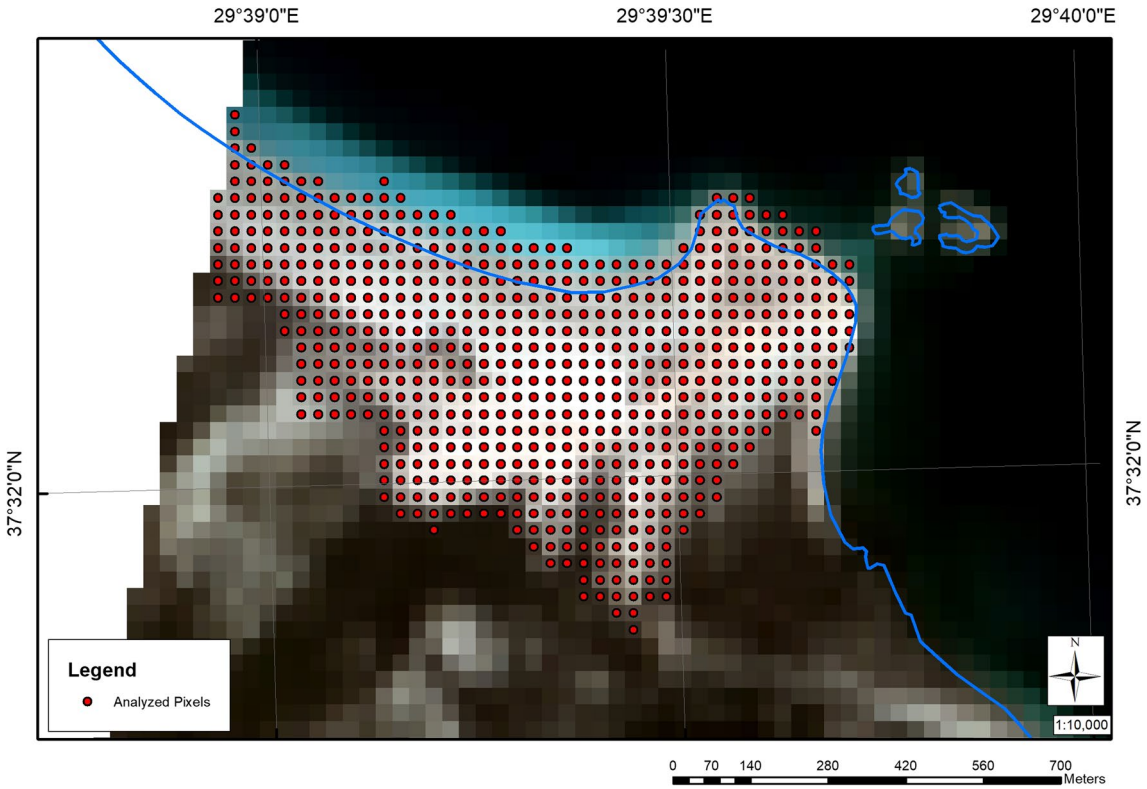

Fig. 5 Map showing the location of pixels

are produced in a limited number of countries. Türkiye has the largest reserves of borax, ulexite, and colemanite in the world (Helvacı, 2019b).

The distribution of tincalconite ($Na_2(B_4O_7)\ 5H_2O$) detected in 19.6% of the study area is shown in Fig. 8c. It is a hydrous sodium borate mineral closely related to borax and is a secondary mineral formed as a dehydration product of borax (Anthony et al. 2003). Tincalconite is typically found as a fine-grained white powder. It is formed when borax is exposed to air and decomposes (Helvaci et al. 2017), as well as naturally occurring, such as in Searles Lake, California. It has been found in California, USA; Salta, Argentina; Eskisehir, Türkiye; Tuscany, Italy; and the Kerch Peninsula, Ukraine (Anthony et al. 2003).

The distribution of vermiculite ($(Mg, Fe^{+2},Al)_3((Al,Si)_4O_{10})(OH)_2\ 4H_2O$) detected in 9.8% of the study area is presented in Fig. 8d. In vermiculite minerals, which are expandable phyllosilicates, the Fe oxidation state is directly affected by both external redox conditions and microbial activities. These reactions are important for microbial respiration and, more generally, in soils where water saturation conditions, microbial activity, and organic matter concentrations modify the Fe oxidation state in phyllosilicates (Cuadros et al. 2019). An alteration product of biotite or phlogopite by weathering or hydrothermal action. Formed at the contact between felsic and mafic or ultramafic rocks, such as pyroxenites and dunites, and in carbonatites and metamorphosed limestones (Anthony et al. 2003).

The distribution of colemanite ($Ca_2B_6O_{11}\ 5H_2O$) detected in 7.1% of the study area is shown in Fig. 8e. A common constituent in borate deposits formed in arid alkaline lacustrine environments, deficient in sodium and carbonate, typically under warm conditions (Anthony et al. 2003). Borax, ulexite, and colemanite, which are the most commercially dominant and most important borate minerals worldwide, are produced in a limited number of countries, essentially by Türkiye and the United States. These minerals are largely a constituent of economic nonmarine evaporates formed concentrated in continental Tertiary deposits of western Anatolia (Türkiye) and the American continents (Helvacı et al. 2017).

Rivadavite, a hydrated sodium and magnesium borate, was detected in 5.0% of the study area and its distribution is shown in Fig. 8f. The mineral, which is found in sedimentary borate deposits and deposited from borate-rich hot springs, has been identified in the Salta region of Argentina, the California region of the USA, and the Balıkesir region of Türkiye (Anthony et al. 2003).

The Karakova Stream and its tributaries, descending from the hills up to 2050 m high around Salda Lake, carry eroded materials with high energy and form the Karakova fan delta in the study area. Magnesium and sodium concentrations

Table 3 Results of ACE analysis

Number	Mineral	Max value	Mean value	Std dev	The number of Pixels	Perc. (%)	Chemical formula (Korbel and Novák 2001; Chukanov 2014; Kokaly et al. 2017)
1	Trona GDS148	0.86	0.68	0.15	222	35.0	$Na_3(CO_3)(HCO_3)\ 2H_2O$
2	Ulexite HS441.3B	0.81	0.67	0.14	166	26.2	$NaCaB_5O_9\ 8H_2O$
3	Tincalconite GDS142	0.82	0.66	0.14	124	19.6	$Na_2B_4O_7\ 5H_2O$
4	Vermiculite VTx-1.a < 250	0.79	0.65	0.13	62	9.8	$(Mg,Fe^{+2},Al)_3(Al,Si)_4O_{10}(OH)_2\ 4H_2O$
5	Colemanite GDS143	0.79	0.64	0.13	45	7.1	$Ca_2B_6O_{11}\ 5H_2O$
6	Vermiculite VTx-1.fls	0.79	0.63	0.14	39	6.2	$(Mg,Fe^{+2},Al)_3(Al,Si)_4O_{10}(OH)_2\ 4H_2O$
7	Rivadavite NMNH170164 Amph	0.78	0.64	0.13	32	5.0	$Na_6MgB_{24}O_{40}\ 22H_2O$
8	Bloedite GDS147	0.77	0.64	0.13	29	4.6	$Na_2Mg(SO_4)_2\ 4H_2O$
9	Kainite NMNH83904	0.79	0.63	0.13	26	4.1	$MgSO_4\ KCl\ 3H_2O$
10	Vermiculite GDS13 Llano	0.80	0.65	0.14	25	3.9	$(Mg,Fe^{+2},Al)_3(Al,Si)_4O_{10}(OH)_2\ 4H_2O$
11	Clinoptilolite GDS152 Zeolit	0.77	0.64	0.14	20	3.2	$(Na,K,Ca)_{2\text{-}3}Al_3(Al,Si)_2Si_{13}O_{36}\ 12H_2O$
12	Opal WS732	0.79	0.61	0.15	15	2.4	$SiO_2\ nH_2O$
13	Sodium_Bicarbonate GDS55	0.80	0.59	0.16	11	1.7	$NaHCO_3$
14	Ulexite GDS138 Boron; CA	0.79	0.61	0.13	10	1.6	$NaCaB_5O_9\ 8H_2O$
15	Pinnoite NMNH123943	0.78	0.62	0.13	5	0.8	$MgB_2O_4\ 3H_2O$
16	Sepiolite SepNev-1.AcB	0.78	0.63	0.13	5	0.8	$Mg_4Si_6O_{15}(OH)_2\ H_2O$
17	Sepiolite SepSp-1.AcB	0.76	0.6	0.15	3	0.5	$Mg_4Si_6O_{15}(OH)_2\ H_2O$
18	Opal TM8896 (Hyalite)	0.78	0.61	0.12	2	0.3	$SiO_2\ nH_2O$
19	Saponite SapCa-1.AcB	0.75	0.59	0.14	2	0.3	$(½Ca,Na)_{0.33}(Mg,Fe^{+2})_3(Si,Al)_4O_{10}(OH)_2\ 4H_2O$
20	Sepiolite SepNev-1	0.78	0.62	0.13	1	0.2	$Mg_4Si_6O_{15}(OH)_2\ H_2O$
21	Epsomite GDS149	0.76	0.56	0.12	1	0.2	$MgSO_4\ 7H_2O$
22	Saponite SapCa-1	0.76	0.61	0.14	1	0.2	$(½Ca,Na)_{0.33}(Mg,Fe^{+2})_3(Si,Al)_4O_{10}(OH)_2\ 4H_2O$
23	Bassanite GDS145	0.75	0.59	0.12	1	0.2	$2CaSO_4\ H_2O$

in wells and cold water springs in the ultramafic surroundings of the lake average 60 ppm and 5 ppm, respectively. Temperature and pH vary between 12–15 °C and 8–10, respectively (Zedef 1994; Braithwaite and Zedef 1996). Water samples collected from the lake surface and up to a depth of 80 m always contained 300 ppm Mg and 200 ppm Na at pH 9.1. After evaporation and precipitation of alkaline earth carbonate minerals, they transform into high pH magnesium carbonate brines that precipitate hydromagnesite ($Mg_5(CO_3)_4(OH)_2•4H_2O$) (Russell, 1999). High pH sodium carbonate brines can also cause trona ($Na_2CO_3\ NaHCO_3\ 2H_2O$) to precipitate. Helvacı (1998) reported the presence of magnesite ($MgCO_3$) in the Beypazarı/Türkiye trona field.

Conclusion

Understanding the historical process of Mars, which used to have water and is now arid, is important for predicting the future of our planet. However, although these studies on Mars are carried out with the help of expensive satellites, landers, and rovers, they remain weak in comparison with the studies to be carried out on Earth. Instead of the Jezero crater on Mars, it is essential to make detailed analyzes in Lake Salda, which is similar to it in our world, not only to understand the history of our Earth, but also to understand the history of Mars.

Collecting representative samples in a large area of approximately 57 hectares in Salda Lake brings with it many difficulties in terms of time, cost and manpower, and in a protected area, such activities can even harm the area in terms of research. Therefore, remote sensing applications are particularly useful especially in protected areas such as Lake Salda limits the direct geological exploration. It is concluded that EO-1 Hyperion satellite observations will help to better understand the mineralogical characteristics of the Salda Lake surroundings. In this study, mineral analysis was performed using remote sensing methods without damaging such a specially protected sensitive area.

Analysis reveals that the examined area consists of hydromagnesite along with trona and borates such as ulexite, tincalconite and colemanite. Hydromagnesite is

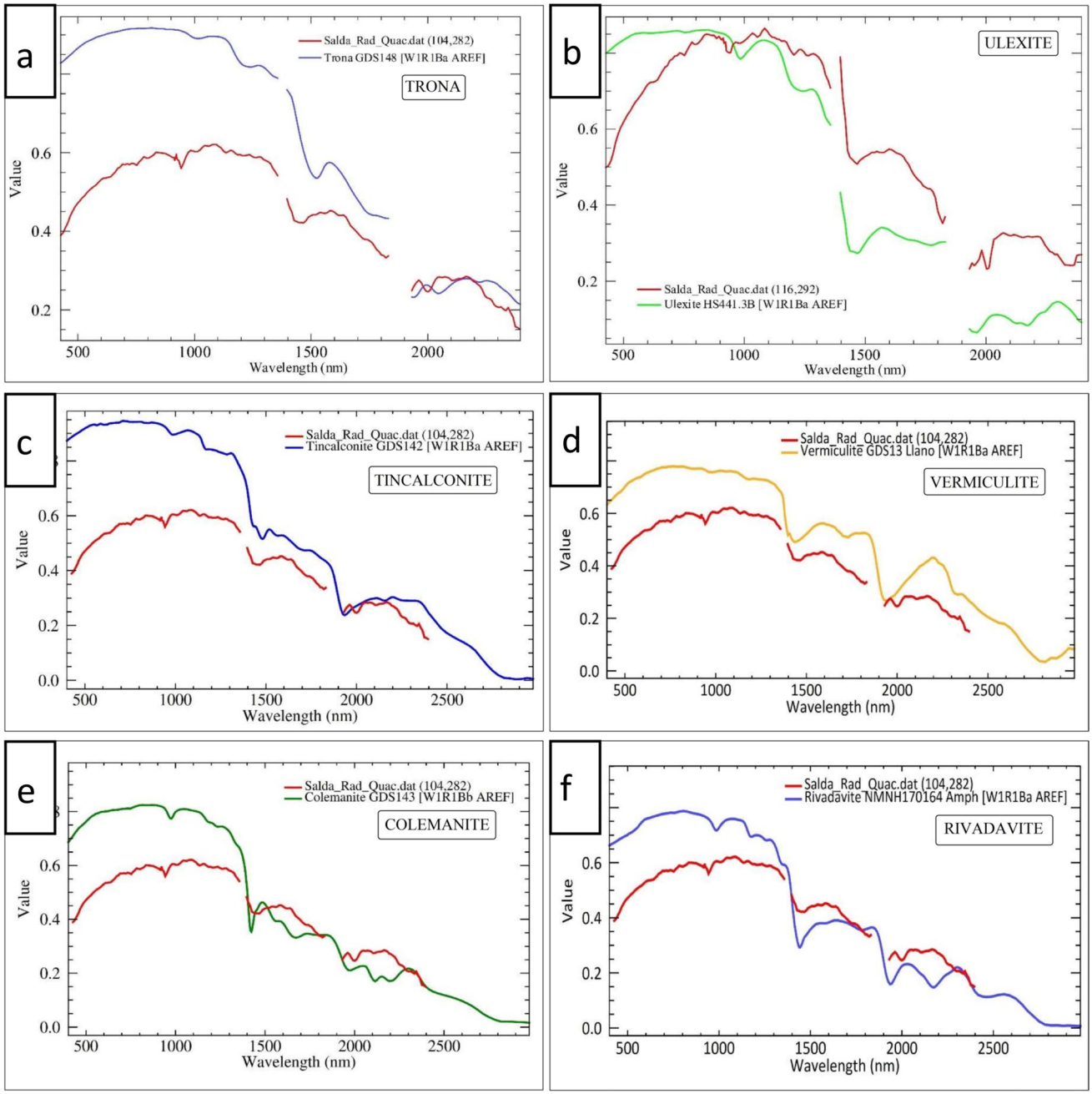

Fig. 6 The wavelength graphs of the six minerals that have a distribution greater than 5% in the study area

the most abundant minerals in the study area. As a result of mineral analysis using the Hyperion satellite with hyperspectral detection, 35% trona, 26.2% ulexite, 19.6% tincalconite, 9.8% vermiculite, 7.1% colemanite and 5.0% rivadavit minerals were detected on the surface of the 57-hectare study area.

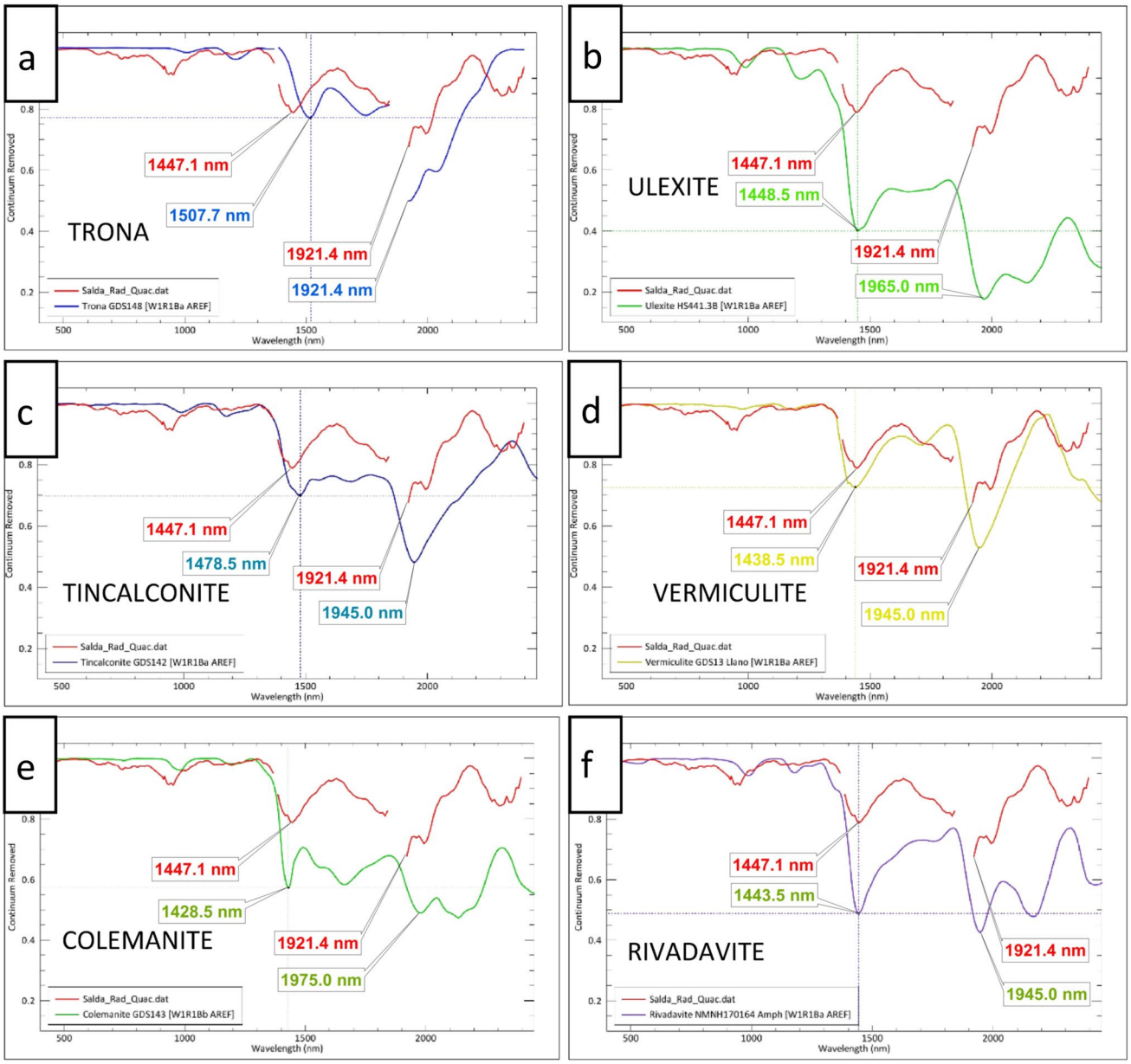

Fig. 7 The Continuum Removed graph in the pixel with the highest ACE values of the six minerals

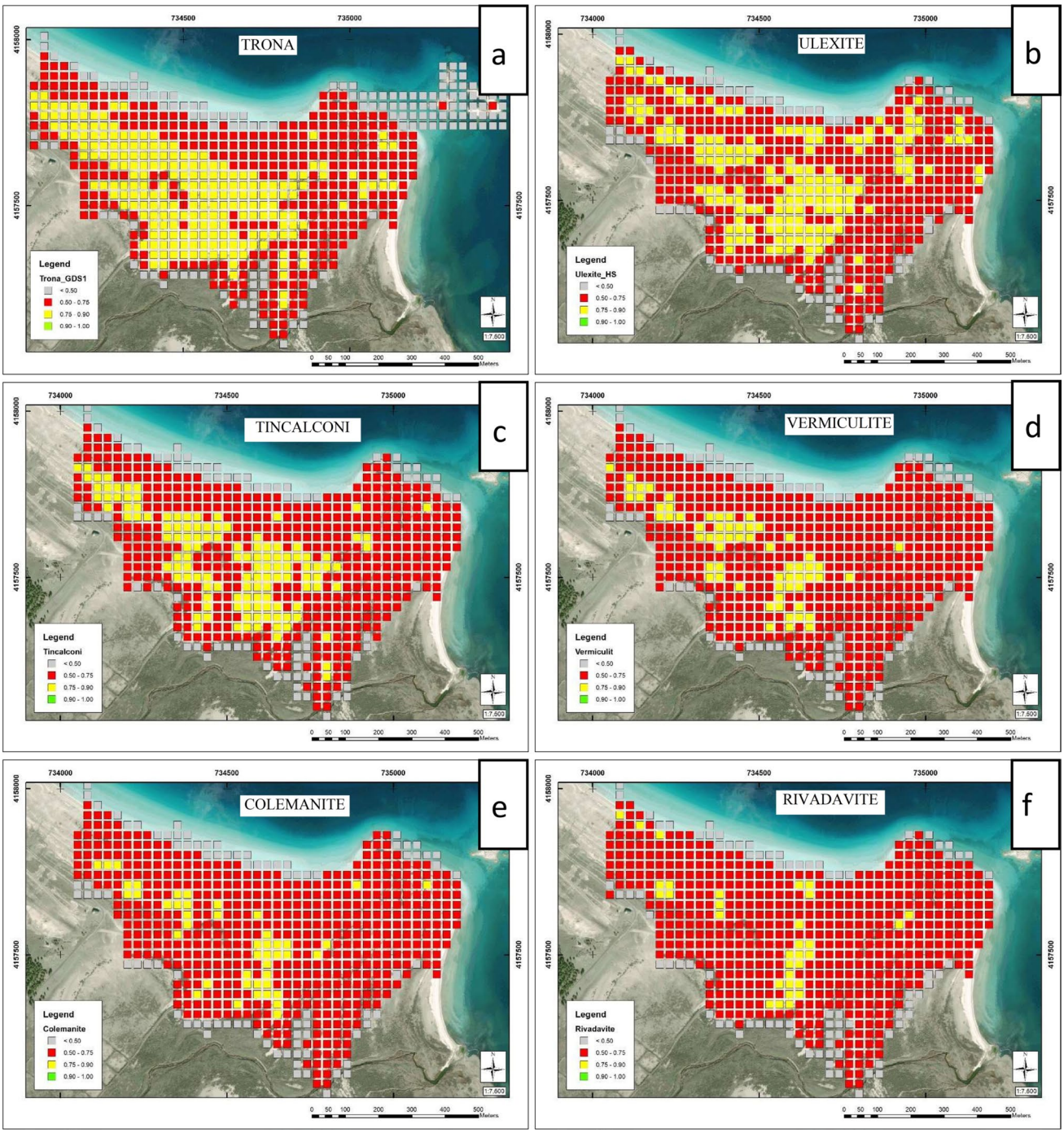

Fig. 8 Distribution maps of the six minerals

Author contributions Conceptualization, methodology, software, formal analysis, data curation, writing—original draft, writing—review and editing were performed by MAA. Conceptualization, methodology, software, formal analysis, data curation, writing—review and editing were performed by SU. All authors read and approved the final manuscript.

Funding Open access funding provided by the Scientific and Technological Research Council of Türkiye (TÜBİTAK). The authors received no funding for this work.

Data availability The data that support the findings of this study are available from the corresponding author, upon reasonable request.

Declarations

Conflict of interest The authors have no competing interests to declare that are relevant to the content of this article.

Open Access This article is licensed under a Creative Commons Attribution 4.0 International License, which permits use, sharing, adaptation, distribution and reproduction in any medium or format, as long as you give appropriate credit to the original author(s) and the source, provide a link to the Creative Commons licence, and indicate if changes were made. The images or other third party material in this article are included in the article's Creative Commons licence, unless indicated otherwise in a credit line to the material. If material is not included in the article's Creative Commons licence and your intended use is not permitted by statutory regulation or exceeds the permitted use, you will need to obtain permission directly from the copyright holder. To view a copy of this licence, visit http://creativecommons.org/licenses/by/4.0/.

References

Akkuş A (1987) Salda lake geomorphology, Istanbul University. J Geogr sayı:2, sayfa:109–115 **(in Turkish)**

Altınlı E (1955) The geology of Southern Denizli. İstanbul Üniversitesi Fen Edebiyat Fakültesi Mec. Seri B, XX, No:1–2, sayfa:1–45, İstanbul

Anthony JW, Bideaux RA, Bladh KW, Nichols MC (Eds.) (2003) Handbook of mineralogy. Mineralogical Society of America, Chantilly. http://www.handbookofmineralogy.org/

Balcı N, Demirel C, Kurt MA (2018) Geomicrobiology of Lake Salda and microbial influences on present-day stromatolite formation. Bull Earth Sci Appl Res Centre Hacettepe Univ 39(1):19–40

Barry P (2001) EO-1/Hyperion science data user's guide. TRW Space, Defense & Information Systems

Beck R (2003) EO-1 User Guide v.2.3; University of Cincinnati, Cincinnati, p 74

Bernstein LS, Adler-Golden SM, Sundberg RL, Levine RY, Perkins TC, Berk A, Ratkowski AJ, Felde G, Hoke ML (2005) Validation of the QUick Atmospheric Correction (QUAC) algorithm for VNIR-SWIR multi- and hyperspectral imagery. In: SPIE, Proceedings, Algorithms and Technologies for Multispectral, Hyperspectral, and Ultraspectral Imagery XI. Vol. 5806, pp 668–678

Bernstein LS, Jin X, Gregor B, Adler-Golden SM (2012) Quick atmospheric correction code: algorithm description and recent upgrades. Opt Eng 51(11):111719. https://doi.org/10.1117/1.OE.51.11.111719

Bouzidi W, Mezned N, Abdeljaoued S (2022) Mineralogical mapping using EO-1 Hyperion data for iron mine identification. J Appl Remote Sens 16(2):024514–024514. https://doi.org/10.1117/1.JRS.16.024514

Braithwaite CJR, Zedef V (1996) Living hydromagnesite stromatolites from Turkey. Sed Geol 92:1–5

Canty JM (2014) Image analysis, classification and change detection in remote sensing, with algorithms for ENVI/IDL and Python, 3rd edn. CRC Press, Boca Raton

Chukanov NV (2014) IR spectra of minerals and reference samples data. Infrared spectra of mineral species. Springer Geochemistry/Mineralogy. Springer, Dordrecht. https://doi.org/10.1007/978-94-007-7128-4_2

Clark RN, Roush TL (1984) Reflectance spectroscopy: quantitative analysis techniques for remote sensing applications. J Geophys Res 89(B7):6329. https://doi.org/10.1029/JB089iB07p06329

Clark RN, Swayze GA, Wise R, Livo E, Hoefen T, Kokaly R, Sutley SJ (2007) USGS digital spectral library splib06a. U.S. Geological Survey, Digital Data Series, p 231. http://speclab.cr.usgs.gov/spectral.lib06

Cuadros J, Michalski JR, Dyar MD, Dekov V (2019) Controls on tetrahedral Fe(III) abundance in 2:1 phyllosilicates. Am Miner 104:1608–1619. https://doi.org/10.2138/am-2019-7036

Datt B, McVicar TR, Van Niel TG, Jupp DLB (2003) Preprocessing EO-1 hyperion hyperspectral data to support the application of agricultural indexes. IEEE Trans Geosci Remote Sens 41(6):1246–1259. https://doi.org/10.1109/TGRS.2003.813206

Ducart DF, Silva AM, Toledo CLB, Assis LM (2016) Mapping iron oxides with Landsat–/OLI and EO-1/Hyperion imagery from the Serra Norte iron deposits in the Carajás Mineral Province, Brazil. Braz J Geol 46(3):331–349. https://doi.org/10.1590/2317-4889201620160023

Erentöz C (1974) Geological map of Türkiye (Denizli), 1/500000 scale. MTA Publications, Ankara ((**in Turkish**))

ESRI (2011) ArcGIS desktop: release 10. Environmental Systems Research Institute, Redlands

Garczynski B, Horgan B, Kah LC, Balci N, Gunes Y (2019) Searching for potential biosignatures in jezero crater with Mars 2020—a spectral investigation of terrestrial lacustrine carbonate analogs. In: Ninth international conference on Mars 2019, (LPI Contrib. No. 2089)

Helvacı C (1998) The Beypazari trona deposit, Ankara Province, Turkey. In: Proceedings of the first international soda ash conference: Wyoming State Geological Survey Public Information Circular 40

Helvacı C (2019a) Turkish trona deposits: geological setting, genesis and overview of the deposits. In: Pirajno F, Ünlü T, Dönmez C, Şahin M (eds) Mineral resources of Turkey. Modern approaches in solid earth sciences, vol 16. Springer, Cham. https://doi.org/10.1007/978-3-030-02950-0_12

Helvacı C (2019b) Turkish borate deposits: geological setting, genesis and overview of the deposits. In: Pirajno F, Ünlü T, Dönmez C, Şahin M (eds) Mineral resources of turkey modern approaches in solid earth sciences, vol 16. Springer, Cham. https://doi.org/10.1007/978-3-030-02950-0_11

Helvacı C, Öztürk YY, Emmermann A (2017) Fluorescence survey of Turkish borate minerals: comparative measurements of fluorescence spectra of the most important borate mineral species, Turkey. Neues Jahrbuch Mineral Abhandl J Mineral Geochem 194:1–17

Horgan BHN, Anderson RB, Dromart G, Amador ES, Rice MS (2020) The mineral diversity of Jezero crater: evidence for possible lacustrine carbonates on Mars. Icarus 339:113526. https://doi.org/10.1016/j.icarus.2019.113526

Kah LC, Balci N, Gunes Y, Williford KH, Cloutis EA (2020) Investigating the origin of carbonate deposits in jezero crater: mineralogy of a fluviolacustrine analog at Lake Salda, Turkey. In: 51st Lunar and planetary science conference

Kaya M, Yildirim BA, Kumral M, Sasmaz A (2023) Trace and Rare Earth Element (REE) geochemistry of recently formed stromatolites at Lake Salda, SW Turkey. Water 15:733. https://doi.org/10.3390/w1504073

Kazancı N, Girgin S, Dügel M (2004) On the limnology of Salda Lake, a large and deep soda lake in southwestern Turkey: future management proposals. Aquat Conserv Mar Freshw Ecosyst 1:151–162

Kokaly RF, Clark RN, Swayze GA, Livo KE, Hoefen TM, Pearson NC, Wise RA, Benzel WM, Lowers HA, Driscoll RL, Klein AJ (2017) USGS spectral library version 7: U.S. Geological Survey Data Series 1035, p 61. https://doi.org/10.3133/ds1035

Korbel P, Novák M (2001) The complete Encyclopedia of minerals. Grange Books PLC, UK

Kraut S, Scharf LL, Butler RW (2005) The adaptive coherence estimator: a uniformly most-powerful-invariant adaptive detection statistic. IEEE Trans Signal Process 53(2):427–438. https://doi.org/10.1109/TSP.2004.840823

Manolakis D, Marden D, Shaw GA (2003) Hyperspectral image processing for automatic target detection applications. Lincoln Lab J 14(2003):79–116

MTA (2023) https://www.mta.gov.tr/v3.0/sayfalar/hizmetler/doc/DENIZLI.pdf. Accessed 01 July 2023

NASA (2023) Catalog of spaceborne imaging, nasa space science data coordinated archive (NSSDC), NASA Goddard Space Flight Center (GSFC), https://nssdc.gsfc.nasa.gov/. Accessed 01 July 2023

Nv5 (2023) Hyperspectral material identification, https://www.nv5geospatialsoftware.com/docs/thorhyperspectralmaterialidentification.html. Accessed 03 Aug 2023

Oskouei MM, Babakan S (2016) Role of smile correction in mineral detection on hyperion data. J Min Environ 7(2):261–272. https://doi.org/10.22044/jme.2016.567

Pour AB, Hashim M (2014) Alteration mineral mapping using ETM+ and hyperion remote sensing data at Bau Gold Field, Sarawak, Malaysia. In: IOP conference series: earth and environmental science, vol 18, 8th International Symposium of the Digital Earth (ISDE8) 26–29 August 2013, Kuching, Sarawak, Malaysia.https://doi.org/10.1088/1755-1315/18/1/012149

Russell MJ, Ingham JK, Zedef V, Maktav D, Sunar F, Hall AJ, Fallick AE (1999) Search for signs of ancient life on Mars: expectations from hydromagnesite microbialites, Salda Lake, Turkey. J Geol Soc 156:869–888. https://doi.org/10.1144/gsjgs.156.5.0869

Salaj SS, Upadhyay R, Srivastav SK, Prabhakaran N (2012) Mineral abundance mapping using hyperion dataset in part of Udaipur Dist Rajasthan India. In: Proc. Annu. Int. Conf. Exhib. Geospatial Inf. Technol. Appl., pp 1–14

Simon K, Beckman T (2006) Hyperion Level 1G (L1GST) product output files data format control book (DFCB), Earth observing-1 (EO-1), version 1.0, USGS Center for Earth Resource Observation and Science (EROS), Sioux Falls, South Dakota

USGS (2021) EO1 data dictionary. Earth resources observation and science (EROS) Center July 2, 2021. https://www.usgs.gov/centers/eros/science/eo1-data-dictionary

USGS (2023) Earth explorer. https://earthexplorer.usgs.gov/. Accessed 20 May 2023

Varol S, Küçük M, Davraz A, Şener Ş, Şener E, Aksever F, Kırkan B, Tokgözlü A (2020) Investigation of the hydrogeology and hydrogeochemical properties of the South of the Salda Lake Basin. J Eng Sci Des (Yeşilova/Burdur) 8(1):74–90

Wang ZG, Zheng CY (2010) Rocks/minerals information extraction from EO-1 Hyperion data base on SVM. In: 2010 International conference on intelligent computation technology and automation, Changsha, China, 2010, pp 229–232. https://doi.org/10.1109/ICICTA.2010.341

Wolfe JD, Black SR (2018) Hyperspectral analytics in ENVI: target detection and spectral mapping methods. Harris Corporation, September 19, 2018 Edition

Zedef V (1994) The origin of magnesite in Turkey, a stable isotope study. PhD Thesis, Glasgow University

Publisher's Note Springer Nature remains neutral with regard to jurisdictional claims in published maps and institutional affiliations.